Wind Turbine Team at Virginia Tech

Technical Design Written Report

2021 U.S. Department of Energy Collegiate Wind Competition
Virginia Tech

Blacksburg, Virginia, WindTurbineTeamVT@vt.edu
Twitter/Instagram/Facebook: @WindTurbineTeamVT

Team Leads
Alvaro Armaza (Project Manager) | **Hayley Capilitan** (Project Manager)
Christina Watt (Siting & Business) | **Kai Kato & Om Shah** (Mechanical)
Benjamin Alden (Power Systems and Controls) | **Elizabeth Spicer** (Blades)

Advisors
Dr. Matthew Kuester (Principal Investigator, Department of Aerospace Engineering)
Dr. Arthur Ball (Assistant Investigator, Department of Electrical and Computer Engineering)

Members: 33 (8 majors), Advisors: 2

COLLEGIATE WIND COMPETITION
U.S. DEPARTMENT OF ENERGY

VIRGINIA TECH

maxon

Table of Contents

Contents

Executive Summary

Following the effects of COVID-19 on the Collegiate Wind Competition in 2019-2020, the Wind Turbine Team at Virginia Tech sought to use the restricted nature of this year's competition as an opportunity to focus on the fundamentals of design with an emphasis on simplicity and validation. With both of these facets of design in mind; the team was able to rely on returning team members to complete designs previously started and integrate new subsystems and blade manufacturing that would pave the way for us to think differently than in past years.

With distributed manufacturing and uncertainty being a principle of this year's competition, the team had to have contingency plans in place to accommodate any unforeseen circumstances that would impede the production of our turbine. The team aimed to minimize any outsourcing needed through the use of machining labs at the Virginia Tech campus and a makerspace provided to us by the Aerospace and Ocean Engineering Department. Through planning and scheduling, duly documentation, minimizing outsourcing, and staying up long hours to come up with creative solutions, the team was proudly able to produce a wind turbine prototype.

The team began our design exploring new methods to manufacture blades. The final method was chosen to be a fiberglass wrapped blade coated in epoxy with a balsa wood structure. This provided a reliably iterative approach to making blades given most resources could be gathered from hardware stores.

A focus on reliability and safety was emphasized in our mechanical systems. Our pre-existing pitch control and hub was validated using Finite Element Analysis, load bearing calculations and testing in a wind tunnel. A mechanical brake was integrated for Safety task to effectively reduce the rotational inertia of the turbine and to avoid using a power systems and controls related approach to directly slow the turbine down. Continuing our theme of simplicity, a passive yaw was used for Durability Task as an active system would add complexity to the wind turbine.

The power systems and controls of our wind turbine followed a shift towards simplicity and remote design by lessening the number of circuits and using more digital controls. A DC permanent magnet generator was chosen to eliminate the need for a rectifier. An *Arduino Uno* was used as the digital controller to accommodate a preference of signals over using less power in a microcontroller for a simpler system.

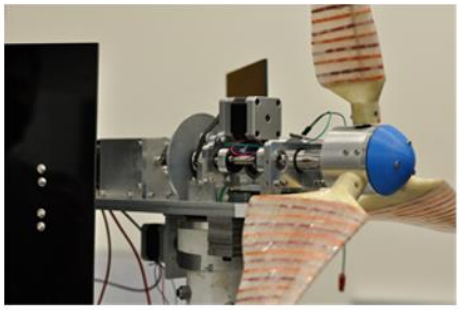

Figure 1. Final Virginia Tech turbine design

Our final testing results showed that we were able to accomplish our goals of validation and simplicity to produce a functioning turbine. The turbine was able to successfully complete the Cut-In, Power Curve, and Durability tasks, Additionally, for the first time ever the team was able to acquire points in Safety task through the addition of a mechanical brake. Not all the tasks were completed as expected, however the performance of our turbine gives us hope that a simple design paired with the resources we will have in a non-COVID-19 environment will be the drivers of new heights reached in the coming year.

Enumeration of Pre-Existing Subsystems

1. Blade Pitch Control System and Blade Hub
2. In-house Blade Element Momentum Theory Code for Blade Design
3. Two-tailed Passive Yaw
4. Tower/Bearing

Blades

Blade Design

This year, we aimed to create blades in a distributed manufacturing environment. Because of changes at Virginia Tech brought on by COVID-19, we had limited access to 3D printers to manufacture blades. Therefore, our main objective was to explore different materials and manufacturing methods to make our turbine blades with minimal outsourcing and specialty materials. The team also sought to improve blade performance, specifically power production across various wind speeds, by comparing two methods of blade design.

Across the course of the 2020-2021 academic year, we created three sets of blades in an attempt to achieve our two goals. Blade design was driven by power curve matching, as the turbine's generator was selected early in the design process. We focused on maximizing performance at low wind speeds by selecting root and tip airfoil combinations that maximized the largest lift-to-drag coefficient ratio. We designed our first and second set of blades using our in-house Blade Element Momentum Theory (BEMT) MATLAB optimization code. We designed our third set using a more manual approach that will be described later in the report. Each set of blades were designed to operate at tip speed ratios (TSR) between 3 and 4.

All three sets of blades were manufactured largely by hand. Each utilized a wooden cross-sectional structure that we wrapped in fiberglass and coated with an epoxy resin. The second set of blades featured a molded root section made of expanding foam. The third set included a 3D printed root section to ensure the set screws holes for our hub-connecting spars were consistent between all three blades.

Airfoil Selection

For each of our designs, we chose one airfoil for the blade root and another airfoil for the blade tip. We began the selection process by searching for airfoils with large lift-to-drag ratios. For our first blade design, we entered combinations of airfoils into our optimization code and selected the best performing design from the results. However, our second and third blades involved a more rigorous approach to airfoil selection.

We narrowed down our selection by approximating lift-to-drag coefficient ratios for different distances away from the center of the rotor. Effective root airfoils have high ratios at low Reynolds numbers, which benefits cut-in and performance at low wind speeds. Similarly, effective tip airfoils have high ratios at Reynolds numbers that are higher than those at the root. Prioritizing performance at higher Reynolds numbers at the blade tip ideally produces more power at higher wind speeds. Analyzing these ratios shortened our list to two airfoils. We chose the SD 7080 for the root, shown in blue in **Figure 2**, and GOE 195 for the tip, shown in red.

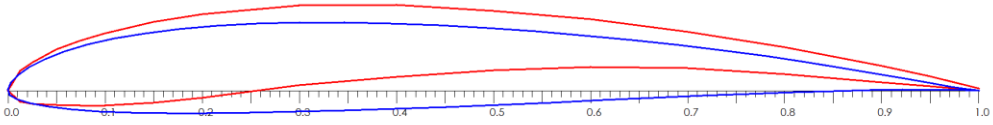

Figure 2. Root and Tip Airfoils

Though each blade utilized one airfoil for the root section and one airfoil for the tip section, each design included a transition section to avoid an abrupt change in cross-section. We used QBlade to create the transition by linearly interpolating between our tip and root foils.

Chord and Twist Design

We utilized two different methods for designing our blades. Like previous years, we began by using our in-house MATLAB BEMT optimization code. [1-5] This code allows the user to specify different blade parameters including the tip speed ratio and geometric constraints. The code aims

to maximize CWC points for the Cut-In and Power Curve tasks by optimizing the twist and chord distribution according to user inputs and a chosen optimization objective. The code has the ability to optimize by prioritizing low cut-in, maximizing power curve performance, or both. The code meets the optimization objectives by cycling through a numerically implemented gradient based optimization algorithm.

We ran the optimization code multiple times to test different combinations of airfoils, initial chord distribution, airfoil transition location, and TSR. Additionally, we utilized the combined optimization objective approach to benefit performance in both Power Curve and Cut-In tasks. The best results from our various trials resulted in Blade Designs 1 and 2, the leftmost blades pictured in **Figure 3**.

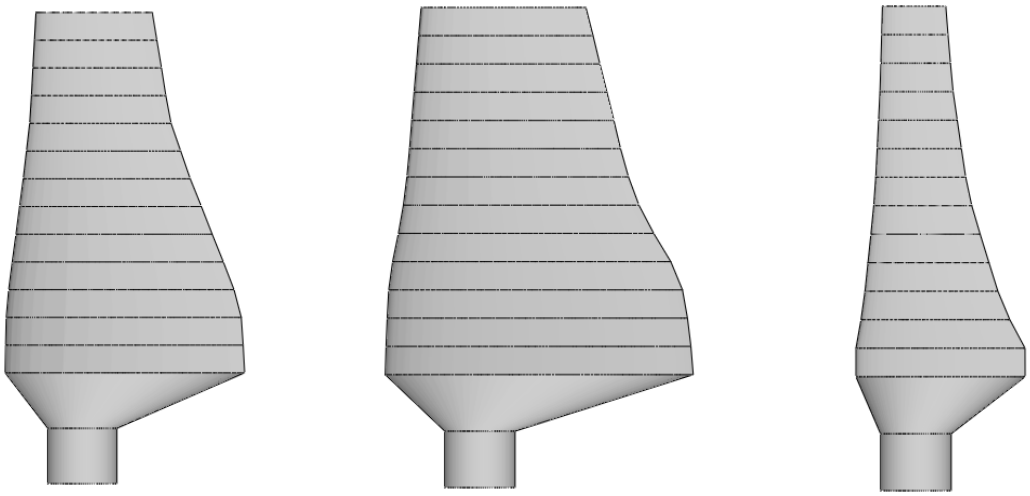

Figure 3. Blade Designs 1, 2, and 3

We present the chord and twist distribution for Blade Design 2, our final design, in **Figure 4**, where radial position represents the distance away from the rotor center. The first two chord length points represent the cylindrical section at the root of the blade where we insert the spar for blade-hub connection.

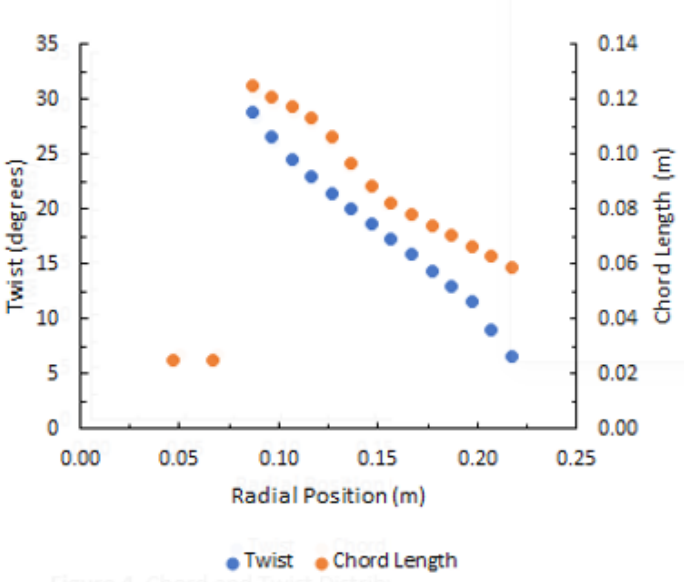

Figure 4. Chord and Twist Distribution of Blade Design 2

This year, we used Betz Optimization as an alternative design method, which involved manually calculating chord and twist values across the length of the blade. We implemented this method to test the validity of our BEMT optimization code after observing differences between predicted and actual power production. More information about these differences will be discussed later in the report.

This manual optimization method utilizes tip speed ratio, selected airfoils, and dimensionless locations to create chord and twist distributions across the blade. The method is designed to maximize power production by first finding the optimal axial and tangential induction factors based on desired criteria. Then, these

induction factors are used to find the chord length and twist at a given radial location that produce maximum power. [6]

We rendered the design in QBlade to easily incorporate a cylindrical region near the root to allow for attachment to the hub. Then, we utilized the linear chord optimization feature to smooth out the geometry and create Blade Design 3 (the rightmost design in **Figure 3**).

The most significant difference between these design methods centers around cut-in wind speed prediction. While BEMT analysis provides a cut-in wind speed for a given design, the simplified approach we took for Blade Design 3 does not. Therefore, we could optimize Power Curve task performance using both methods, but not Cut-In task performance. This difference played a key role in helping us choose our final blade design.

Blade Predicted Performance

We initially analyzed blade performance using our MATLAB BEMT optimization code to find the cut-in wind speed for the turbine with a given blade design and generator. While our first design was predicted to cut-in at 4.43 m/s, our second design was predicted to cut-in at 3.83 m/s. With the manual calculation approach taken for Blade Design 3, we could not easily approximate our cut-in wind speed. Wind tunnel testing proved that this lack of knowledge was detrimental to our turbine's performance. Unfortunately, our third blade design did not achieve cut-in until around 7 m/s, severely impacting performance in both the Cut-In and Power Curve tasks. For these reasons, we opted against using this design.

To predict performance after cut-in, we generated power curves using our MATLAB BEMT code suite and QBlade. **Figure 5** depicts the QBlade-generated blade power curves (solid lines) at various wind speeds for Blade Design 2. The blue markers and trend line represent the generator power curve with a load of 3.98 Ω, the ideal generator load for maximum power production at 6 m/s and 7 m/s. It is important to note that these power curves do not account for electrical and mechanical efficiencies. Instead, we used these curves to approximate performance prior to wind tunnel testing.

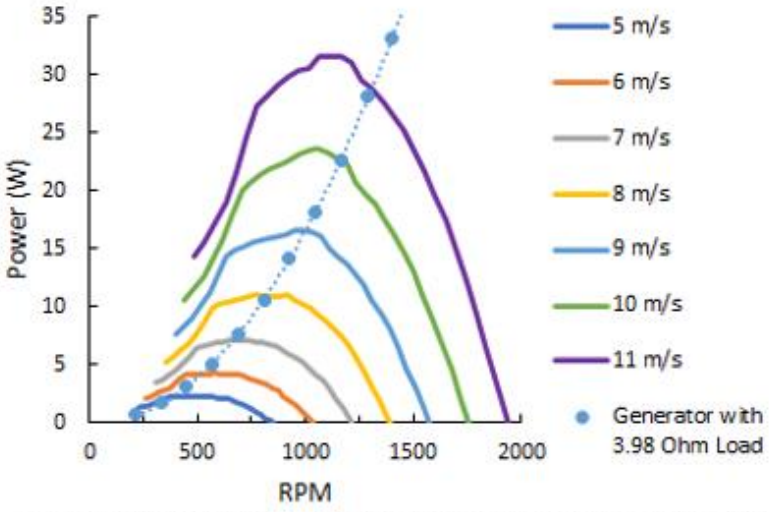

Figure 5. Theoretical blade design 2 power curve from 5 m/s to 11 m/s

We also used the predicted power at each wind speed from **Figure 5** to estimate the annual energy production (AEP). We calculate AEP using Equation 1:

$$AEP = (Operating\ Hours\ Per\ Year) \int_0^\infty (Power)(Probability)\, d(Wind\ Speed) \qquad \text{Eq. 1}$$

The probability term refers to the cumulative probability that a wind speed is between 0 m/s and 11 m/s, calculated using a Weibull distribution:

$$f(V_1 < V < V_2) = exp(-(V_1/A)^k) - exp(-(V_2/A)^k) \qquad \text{Eq. 2}$$

We chose a value of 8.25 m/s for A to represent the average wind speed in Tripp County, the location chosen for Prosim Power's utility scale wind farm and assumed a value of 3 for k. [7]

Using wind speed bins of 1 m/s, we find that our blades should produce 73.178 kWh/year if fully operational for the entire year.

Blade Manufacturing

This year, our team lacked the easy and inexpensive access to fast prototyping methods we used previously. Due to COVID restrictions, among other reasons, we could not feasibly use the high-precision 3D printers on campus and opted for a more hands-on approach to manufacturing. Though our final production method was partially born of necessity, we also aimed to embrace the idea of distributed manufacturing emphasized by this year's competition.

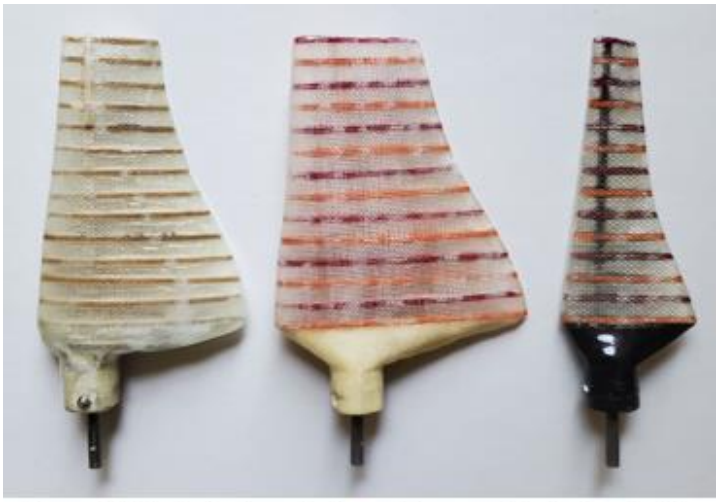

Figure 6. Blade designs 1, 2, and 3, respectively from left to right

Our manufacturing approach for all blades included a wooden skeleton, fiberglass wrap, and epoxy coating. Pictures of each blade can be viewed in **Figure 6** Over time, we made some modifications to the root section of the blade as we gained access to more resources. These modifications allowed for much easier blade-hub connection, something that proved to be extremely important during wind tunnel testing. Despite the increasing sophistication of the root section, we proved that we could create operable blades with minimal resources aside from what can be found at a hardware store.

To reduce the risk associated with implementing a new manufacturing method, we made and tested a set of prototypes that could be attached to the KidWind tower setup (**Figure 7)**. We selected balsa wood to create the cross sections and cut out each piece by hand using a handmade tin stamp and an Exacto knife. We connected each piece using a dowel rod before covering the structure with Bondo fiberglass cloth, which is marketed for strong home, auto, and boat repairs. Then, we used a quick setting epoxy from JB-Weld to create a strong, smooth surface on the blades. These handmade blades withstood preliminary testing at all competition wind speeds, giving us no concerns about structural integrity. At the beginning of this semester, we used the same manufacturing process to create Blade Design 1 with the sole addition of using the laser cutter to create airfoil sections.

Figure 7. Prototype Blades

The blades in our final design (Blade Design 2) feature an expanded foam root section. These silicone-molded sections required less machining to ensure a secure blade-hub connection than our first design. Our final turbine's blades each have a metal blade-hub spar inserted into the expanded foam with a set screw inserted perpendicularly into the spar, anchoring the blade to the hub. We also chose to use a foam with a similar density to the rest of the blade to ensure an even weight distribution and keep the overall weight of the blades low. This manufacturing

method reduced blade weight by 75% in comparison to blades manufactured via rapid prototyping. Though lighter blades do not directly impact the Cut-In or Power Curve tasks, we preferred designs that minimized weight to minimize vibrations, an issue our team has faced in previous years.

Mechanical System

Introduction

The primary goal for our team was to continue the design and validation of the mechanical subsystems that were started in the previous year. For the Control of Rated Power task, we looked to reinforce the pitch control and hub systems. A new mechanical brake was designed to contribute to the Safety task, and we improved the yaw system to perform better during the Durability task.

Due to COVID-19, we had limited access to a lab space and machine shop lead times were long, minimizing the capacity for multiple design iterations. In addition, the mechanical subsystems suffered critical failures in previous years because we failed to validate the designs prior to testing. Therefore, with little room for error and a history of failure, we made it a priority to validate each new design with proper mechanical and aerodynamic loads analysis before proceeding with the manufacturing process.

Pitch Control and Hub

Last year's pitch control system was able to pitch the blades in a total range of 30 degrees which is sufficient for transitioning between the blade's cut-in angle and the power angle. Also, the system had the capability to efficiently control the turbine's rated power with varying wind speeds during the Control of Rated Power task. As a result, we decided to keep the previous year's design, with minor changes to utilize baseplate space more effectively.

Figure 8 shows the pitching system with labeled components. The pitch control system converts translational motion within the drivetrain into rotational motion of the blades. The pitching system operates by mounting a pinion gear **(a)** on each blade and the blades move together with three separate racks **(b)** connections which are all mounted to a single rack attachment **(c)**. The blade pitch angle can be quantified by the rack holder's displacement from its original position. The drive shaft **(d)** is mounted inside an outer aluminum sleeve **(e)** with the rack attachment **(c)** mounted on the hub end **(f)** of the sleeve. The sleeve is then mounted between two radial bearings rotating with the drive shaft. These bearings are fitted inside two aluminum housings **(g)** on the front and rear of the pitch control system. The housings are mounted on lead screws **(h)** which were positioned on either side of the housing's central bearing. As the lead screws rotate, the housing moves forward and backward within the fixed front and rear supports. The linear motion of the housing is transferred to the gear racks inside the hub **(f)**. The lead screws are actuated using a single stepper motor **(i)**; the motor and lead screws have a timing belt pulley **(j)** fastened to their ends, and the timing belt is tensioned between the pulleys. The pulleys are able to transfer the rotational motion of the stepper motor to each lead screw accurately. Additionally, the housings are fastened together by an aluminum bar on their undersides, and a linear rail **(k)** was installed on the bottom of this bar. Two linear carriages **(l)** were mounted to the baseplate of the turbine and the linear rail was inserted into these carriages, allowing the vertical forces and moments to be primarily carried through the linear carriage as opposed to the lead screws.

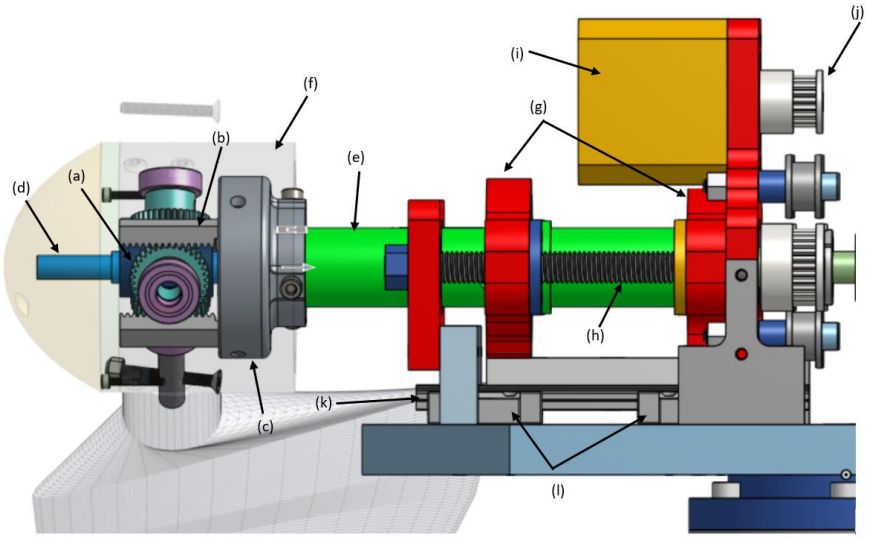

Figure 8. Pitch control assembly with labeled parts

After we concluded that the destructive failures of the hub experienced in previous years were a result of high stress concentrations in its geometry, we decided to prioritize manufacturing and validating the new hub design. We also looked to fortify the hub and pitch control system connection. Last year's rack attachment was a plastic 3D-printed part that mounted the gear racks and also connected to the aluminum sleeve of the pitch control system (design (a) in **Figure 9**). We observed previously that the rack attachment was prone to fracture due to deflection near the base of the gear rack mounting holes.

We aimed to increase the robustness of the design to prevent fracture and better secure the gear rack connection into the hub. We settled on a design with significantly more material and deeper mounting holes to increase the rigidity of the fixed end of the rack and prevent deflection (design (b) in **Figure 9)**.

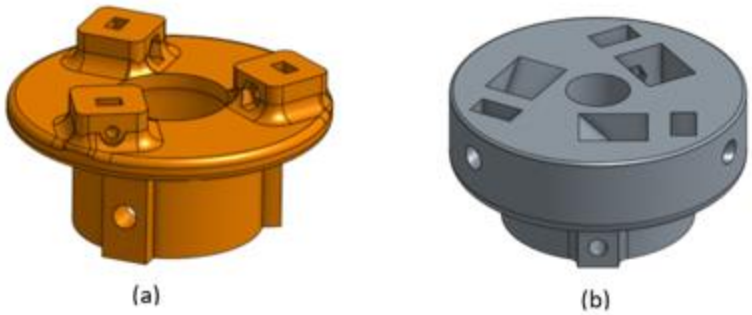

Figure 9. (a) Legacy rack attachment, (b) New rack attachment

The interior geometry of the hub was designed to reduce stress concentrations that were causing cracking near the outer edge of the hub in previous years. In addition, a $\frac{1}{8}$". cylindrical aluminum sleeve was screwed over the exterior of the hub to transfer stresses in the plastic hub core to the metal sleeve and prevent fracturing during testing. We also looked toward the connection between the nose cone and hub, as seen in **Figure 10**. The existing hub required the 3D printed nose cone **(a)** to transfer motion from the hub itself to the drive shaft. The blades generate lift, causing the hub to turn. The hub was attached to the nose cone which was connected to a flanged shaft collar **(b)**. Connecting the shaft collar directly to the hub would require a redesign of the rack blocks, which would require a redesign of the complex interior geometry of the hub. With limitations on manufacturing with COVID-19, we decided against redesigning the shape of the hub because it could have become an iterative process. Instead, we replaced the $\frac{1}{8}$"aluminum sleeve with a $\frac{3}{16}$" sleeve **(d)** to allow space for tapped holes where an aluminum disk **(c)** could be capped on the upwind side of the

hub **(e)**. With this change, the flanged shaft collar can screw directly into the aluminum hub cap, reducing the stresses on the plastic nose cone, ultimately making the part a purely aerodynamic feature.

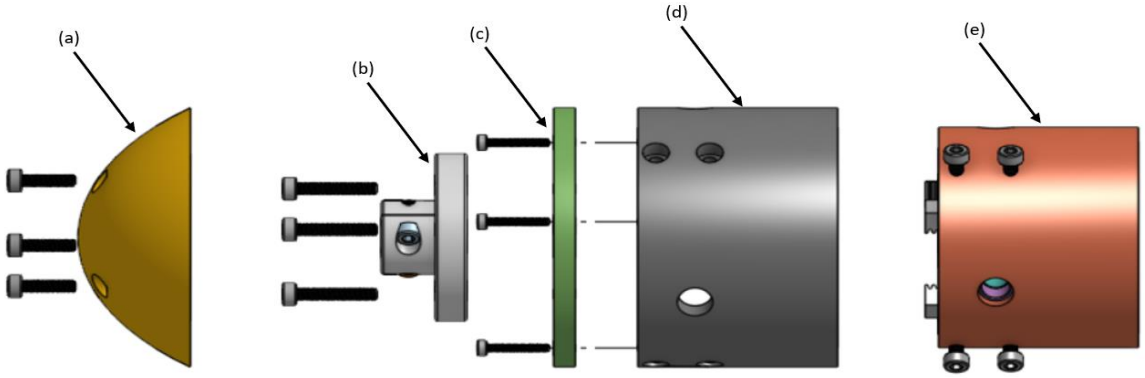

Figure 10. Hub assembly with labeled parts

We continued improvements on the hub by replacing the ¼" hexagonal spars with ¼" circular spars. This format allowed for the use of pinion gears that are sized directly for ¼" spars with machined set screws with better tolerance than the gears we are able to manufacture. Additionally, this allowed us to simplify our assembly by removing the 3D printed hex adapters for each spar. More precise hardware, in conjunction with the use of Loctite, prevented the blades from slipping loose from the hub. To ensure that the redesigned hub would safely operate at the RPMs experienced at the higher wind speed bins, we performed a blade spar loading calculation to determine if the $\frac{3}{16}$" wall thickness would be enough to prevent stress failure at runaway speeds. As seen in the calculations presented in Appendix A, the maximum stress experienced at the inner surface of the spar holes was 6.843 MPa, and the yield strength of the aluminum sleeve was 241 MPa, which yields a factor of safety of 35.22. This calculation included a mechanical and aerodynamic loads analysis at conservative worst-case conditions. The results of the calculations proved that the aluminum provided more than enough reinforcement for the stresses seen from the turbine, deeming the hub design successful.

Considerable testing was done to validate the latest hub design and pitching functions. We conducted preliminary testing by simulating variable rotational speeds while testing the precision and repeatability of the pitch control and rack attachment system. We ran the simulations using our dynamometer fixture, which was constructed last year using 80/20 to run the Rotor Strength test. This year, we used the dynamometer fixture to simulate the turbine spinning when the wind tunnel was unavailable. In the first two wind tunnel testing periods, the hub subsystem was assembled on the turbine and ran under different wind speed bins up to 13 m/s. In the final two testing periods, the hub and pitch control system were present during all competition tasks. In all of the tests, neither system saw any deformations.

Mechanical Brake

To complete the Safety task, our team chose to integrate a mechanical brake system into our wind turbine. The mechanical brake is designed to use friction as a means to reduce the turbine's rotational inertia. As stated in the CWC rules, the turbine is required to slow down to 10% of its rated rpm within 10 seconds. Given our rated RPM of 1100, the target RPM for Safety task is 110 RPM. The rate at which the turbine slows is based on torque, but torque also produces stress in the blades and the hub. To reduce the maximum torque on the rest of the turbine, a minimized, constant braking is best.

First, we selected a style of braking system. Initially, a passive braking system seemed best as it would require no power, ultimately reducing the required hardware needed to control the system. A passive relay system using springs, angled switches, and centripetal force was considered, but the complexity and precision of the system seemed too fine to be realistic. Therefore, an active system seemed like the best option for simplicity. Active systems often face back driving or the system reversing itself to an off position if power is cut off. This means that to keep the system engaged, constant power must be applied. This would require too much power from our system, so a backdriving-resistant system was necessary. One of the simplest methods to prevent back driving is to incorporate a screw in the system with a sufficiently shallow thread angle (Θ) and a sufficiently large coefficient of friction (μ_d). To ensure the validity of our design in preventing backdriving we assessed it under the following relationship:

$$\mu_d > tan(\Theta) \qquad \text{Eq. 3}$$

All of the assessed lead screws met these criteria. Additionally, a screw allows for a conversion of rotational to linear movement which is useful as rotational motors are much stronger and do not have limits on their range of motion when compared with linear actuators.

We designed the rest of the mechanical brake (**Figure**) around this screw **(a)**. We selected a brake disk **(b)** to transfer the point of friction application away from the driveshaft **(c)**. The screw was attached to a mount **(d)** that allowed the screw to rotate. On one end of the screw, we attached a brake pad **(e)** using a carriage **(f)**. We selected a rectangular brake pad to prevent the pad from rotating with the screw and a wide brake pad to decrease the rate of wear. We considered a few ideas to provide a variable pressure to the brake disk to gradually bring the turbine to a stop. Ultimately, we decided that the deflection of the brake disc would control the amount of frictional force applied. Any solid object provides a specific resistance to produce a given deflection based on the geometry and material properties. Using this relationship, if the disc is deflected a specific amount, then the force producing that deflection can be calculated. On the back side of the screw, we attached a pulley **(g)**. This pulley, when combined with a belt, allowed the motor **(h)** to be placed below the baseplate. We added an idler pulley **(i)** to allow custom tensioning of the belt for a more precise control of the pulley system.

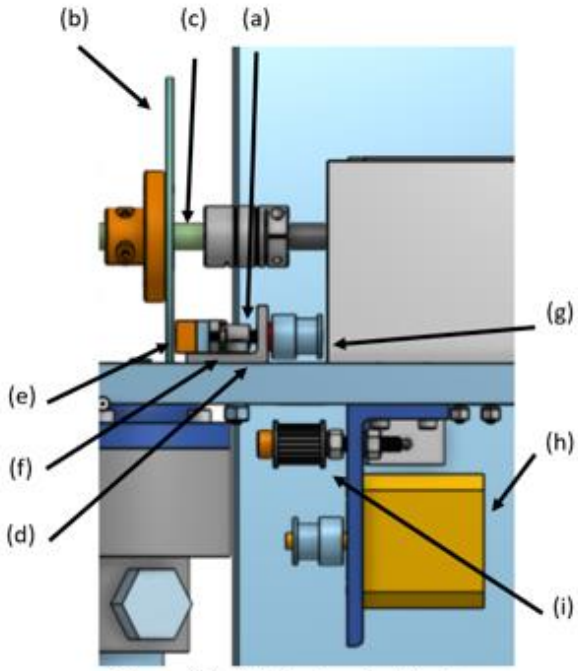

Figure 11. (a) Mechanical brake

With the basic design set out, various components were selected. The stepper motor was selected to be the same as the pitch control motor for ease of integration, low power usage, large torque, and fine step size resolution. We chose aluminum as the brake disc material for its ability to deflect, low density, and durability. To determine the brake pad material, screw thread density, and brake disc thickness, we calculated the necessary amount of friction to brake the system. First, the moment of inertia was calculated using an Onshape CAD model. Next, the distance from the axis of rotation to the center of contact of the brake was calculated. All these values were used in the following stoichiometric equation:

$$\frac{I}{r * \Delta t} * (\alpha_i - \alpha_f) * \frac{2 * \pi\ rads}{rotation} * \frac{1\ min}{60\ sec} \quad \text{Eq. 4}$$

From this equation we found that the necessary braking force was 1.5 N. Based on the pulley ratios and the stepper motor resolution the following equation determined the resolution of the screw rotations to be 0.00625 rotations per step.

$$\frac{1\ rotation\ (motor)}{200\ steps} * \frac{20\ rotations\ (screw)}{16\ rotations\ (motor)} = 0.00625\ rotations\ (screw)\ per\ step \quad \text{Eq. 5}$$

Assuming that the amount that the system can rotate is any integer of steps then the maximum amount of force applied becomes unlimited, but the minimum force resolution becomes an issue so to check the minimum force resolution per step, it is assumed that there is only a single step. Using the minimum resolution criteria, we selected the rest of the specifications. The following equation shows the relationship between the rest of the specifications and the two calculated numbers above.

$$\frac{1.4957\ N}{.00625\ rotations} = \frac{distance}{rotation} * \frac{normal\ force}{distance\ of\ deflection} * \frac{friction\ force}{normal\ force} * factor\ of\ safety \quad \text{Eq. 6}$$

To maximize the factor of safety, the other three factors on the right hand side of the equation must be minimized. The first term relates to how fine the threads on a screw are. We selected the finest threaded lead screw with a distance of 0.5 mm per rotation. The second term is a property of the aluminum disc and is based on the thickness of the disc. To minimize the force required to deflect the disc, we used the thinnest disc that our team could find (0.002 m). Using Solidworks, we conducted an FEA (**Figure 12**) which determined that the deflection of the center of contact of the brake pad is 1100000 N/m. To minimize the final term, the coefficient of friction, we selected a low friction clutch lining with a coefficient of friction of 0.14.

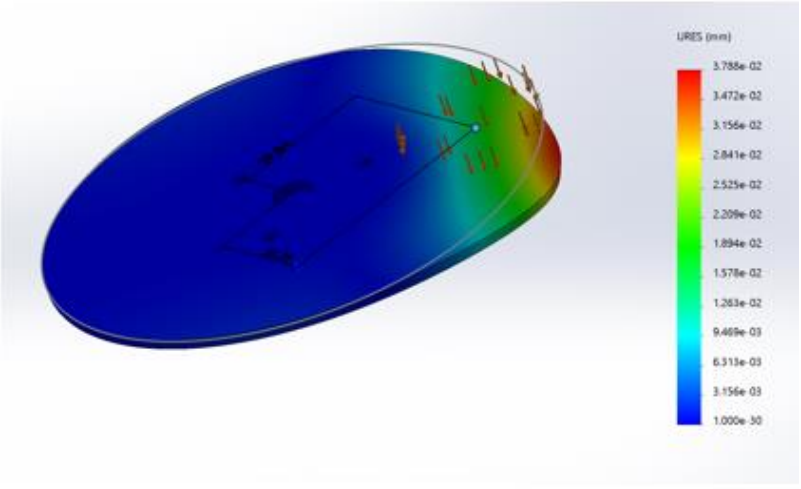

Figure 12. FEA of mechanical brake disc

Using these values and the equation above, we determined the factor of safety to be 3.11. Our initial goal for the factor of safety was set at 3 to ensure that the system would perform as expected if there were unaccounted issues such as slight surface blemishes in the aluminum disc, uneven brake pad force application. This goal was exceeded so the brake disc design was determined to be successful. During testing, given enough time, the mechanical brake was able to completely stop the turbine safely.

Yaw System

We decided to use a passive yaw system to keep the turbine oriented into the wind during the Durability task. The passive system was chosen over an active system because it did not require reliable air direction measurements or an additional motor, allowing for a simpler design. The two-tail design is a continuation of last year's redesign. Testing conducted last year found that the ideal angle for these tails to be mounted was approximately 30°. A MATLAB code was

created to model the torque expected at the yaw bearing from the tail using the approximate mounting locations of the old design. Flat plate lift and drag coefficients were estimated using a calculated Reynolds number, the tail's aspect ratio (b/c where b and c are the tail height and width, respectively), and a range of angles of attacks. From there, force was calculated both parallel and perpendicular to the centerline using the following equations:

$$F_i = .5\rho U^2 bc(-C_L sin(\gamma) + C_D cos(\gamma)) \quad \text{Eq. 7}$$

$$F_j = .5\rho U^2 bc(C_L cos(\gamma) + C_D sin(\gamma)) \quad \text{Eq. 8}$$

where ρ is the air density, U is wind speed, b and c are the height and width of the tail, γ is the angle of the wind to the centerline of the drive system, and C_D and C_L are the drag and lift coefficients. Distances in the i and j directions to a point ¼ up the tail were used to calculate torque, and the final torque was calculated by cross multiplying distance from center of tower to this point on the tail by the force acting on the tail. We summed the torque of each tail (right and left) together for the final torque at each wind angle. As shown in **Figure 13**, 30° was found as the optimal angle between 0° and 40°, validating the experimental results.

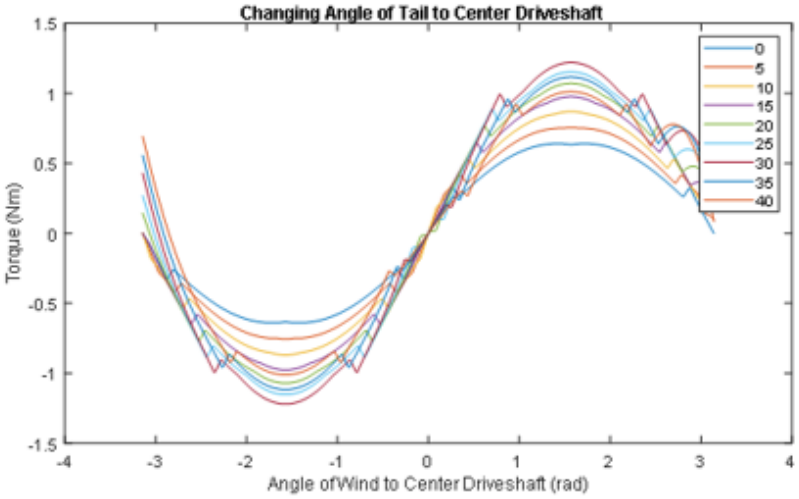

Figure 13. Calculated torques at 10 m/s for winds at -180° to 180° angles with respect to the centerline of the driveshaft.

The new design, shown in **Figure 14**, developed in the spring due to adjustments to the mechanical brake system, shifted the yaw system towards the very back of the baseplate. This caused the mounting beam **(a)** to be split in two and angled to shift the mounting location back farther towards the center of the baseplate. Our team decided to directly mount the yaw tails to the baseplate using two brackets **(b)**, attached above and below an aluminum bar, to attach the tails. This allowed the tails to have a sturdy connection in order to better handle vibrations seen by the large tails which were used to increase our torque and thus the responsiveness of the yaw. To validate and optimize the yaw design, we tested multiple tail sizes **(c)** and mounting angles in the new configuration. After testing the yawing response of the turbine in the wind tunnel, we decided on two 16x30.48 cm tails and two slightly different mounting angles, 25° and 30°. The slight difference between the angles helped compensate for some of the torque generated from the spinning blades and vibrations in the system, which were causing the equilibrium to be slightly off center when the angles were matched. Our final tail combination kept the turbine turned into the wind across all of the operating conditions within +/- 10°. In the future, we may explore an active yaw system, which may respond more accurately to changing wind directions.

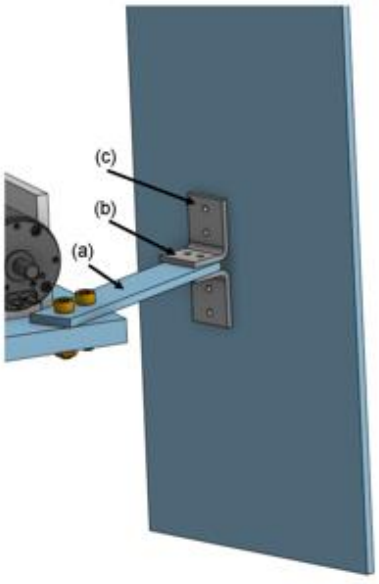

Figure 14. Yaw Assembly (one side)

Vibrations

With more robust subsystems and a larger baseplate, the turbine experienced significant vibrations. In the first two testing periods, we noticed that the turbine would reach its first vibrational mode at wind speeds around 6 m/s and a second mode around 11 m/s. This led us to two conclusions. First, the turbine was experiencing resonance, where the frequency of the blade rotation corresponded to the natural frequency of the turbine. Resonance caused large deflections in the system, which compromised the power output of the turbine and caused the turbine to yaw out of the wind [8]. Second, the source of the vibrations was at the yaw bearing connection between the tower and the baseplate. Due to the weight of the generator and mechanical brake, the turbine's center of gravity was severely imbalanced, favoring the back end of the turbine, causing the bearing to have some mechanical backlash. Initially, to address this issue, we suggested increasing the overall stiffness of the tower; however, after further discussion, we decided against the idea due to the natural frequency of the tower not being reached during operation.

We ultimately decided to add mass to the underside of the baseplate to not only compensate for the center of gravity imbalance, but to act as a damper and lower the natural frequency. We chose to use bars of steel that could be manipulated easily for testing purposes. This added mass was effective at reducing vibrations and maintaining a stable turbine throughout the testing procedures. Ultimately, vibrations on the turbine exposed the major imbalance in the center of gravity of the structure. In the future, we will address this issue at the beginning of the design process.

Power Systems and Controls

Introduction

This year the team focused on minimizing electrical components and subsystems for a simpler design of the electrical and controls systems, embracing the restrictions imposed by COVID-19. This is reflected in the number of circuits implemented. The generator was selected to eliminate the need for DC-DC converters and power regulation methods. To further meet our goals, most controller-based tasks were solved using digital controls as opposed to creating new circuits. A full system schematic may be found in Appendix B for reference.

Generator Selection and Analysis

Generator selection was approached with the goal of achieving 30 W minimum output at rated wind speed and achieving a voltage range to minimize the need for DC-DC converters. 30 W was set as the minimum power output because that is the power achieved in previous years and we did not want to produce less power by changing the generator. Only permanent magnet DC generators were considered. Brushes of a DC generator are not a concern for this application because the turbine is not subject to continuous operation over long periods of time, and thus the wear on the brushes will be minimal. Additionally, using a DC generator removes the need for a rectifier.

Each generator researched by the team was evaluated in the range of 1500 RPM to 2500 RPM, the range of estimated RPM at rated wind speed. The team wanted no more than 24 V at rated RPM to ensure that the 48 V limit would not be exceeded. **Table 1** shows some parameters that were considered when selecting the generator. Rotor inertia was considered as it affects cogging torque and mechanical brake, however it was not weighed as heavily as the electrical characteristics. Low rotor inertia makes it easier for the mechanical brake to stop the turbine and a low cogging torque allows for better cut-in. We used the speed constant to determine the theoretical voltage that the generator would provide at a given RPM. The torque constant was used to determine the approximate amount of torque the blades would need to provide to reach 30 W.

The generator characteristics from each of the researched generators are listed in **Table 1**. These four generators aligned the most with our desired characteristics, and all of the generators are made by Maxon. The RE 50 with 48 V windings was chosen because of its high-speed constant and because it produced no more than 24 V in the estimated RPM range. To obtain the estimated voltage we multiplied the rotor inertia by the Ke value. The rotor inertia for the 48 V RE 50 is high but is only slightly higher than the 24 V RE 50. Given our success in previous years with 24V RE 50, the rotor inertia was deemed acceptable.

Table 1. Generator characteristics from the generator survey.

	RE 50 (48 V)	**RE 35 (48 V)**	**RE 40 (24 V)**	**RE 50 (24 V)**
Rotor Inertia (gcm^2)	542	65.7	119	536
Ke (V/RPM)	0.0093	0.0124	0.00862	0.00403
Torque Constant (A/mNm)	0.0107	0.00840	0.0116	0.0260

Load Design

The ideal resistive load was calculated to be 4.88Ω. We calculated this value based on the RPM at which the blades produce the most power between 6 and 7 m/s, which is 1155 RPM. We can then calculate the load that will make the turbine rotate at the desired RPM. Equation 9 shows how this was calculated:

$$R_{load} = \frac{1}{k^2 C \omega} \quad \text{Eq.9}$$

where,

$$C = \frac{\pi}{2} \rho r^5 \frac{C_P}{\lambda^3} \quad \text{Eq.10}$$

and ρ is the air density, r is the radius of the blades, C_p is the power coefficient, λ is the tip speed ratio, ω is the RPM, and k is the speed constant of the generator. The calculation was done using values for 6-7 m/s since those are the highest weighted bins in the power curve task. We verified this experimentally using different loads from 2.2 Ω to 20 Ω. Our final load selection was 3.98 Ω as this was the closest, we were able to get to 4.88 Ω and produced a better power curve than the other load values tested.

One of the biggest challenges of the CWC is the Safety task, specifically the section that requires restarting the turbine after losing power. To overcome this challenge, we used a resistor and battery in the load. We implemented a latching relay to switch the load from a resistor to a battery and back. Additionally, we designed a relay driver to amplify the signal sent through an optical isolator to switch the relay. To ensure the relay always has enough power to switch, we connected the coils directly to the battery. By connecting the coils directly to the battery, there will be enough power to switch even if the turbine is stopped or producing low power (as is the case at low wind speeds). With a battery in the load, a method to prevent the battery from driving the generator as a motor was needed. Both a diode and generator disconnect were considered. However, a diode was deemed impractical because it would be in the main power path and would constantly dissipate a significant amount of power. A load disconnect was then implemented using a latching relay. Using this method, any time the load was switched to the battery, the generator disconnect relay would also switch to disconnect the generator.

We sized the battery to output approximately 8 V, well within the needed range to power an *Arduino*. The “18650” lithium-ion batteries were selected for their power capacity. These

batteries can power an A*rduino uno* for approximately 65 hours, far longer than needed. However, by having large batteries like this, it ensures that the *Arduino* can stay on and that the rest of our system will have the power needed to operate during the turbine shutdown.

Control of Inputs and Outputs

In order to sample inputs, transition the turbine from one task to the next, and control the pitching system we used a digital control system. Our team selected an *Arduino Uno* as the microcontroller because of the many inputs and outputs in the electrical system. Using more signals was preferred overusing less microcontroller power because each pin had a single function, leading to a simpler system.

To reduce the effects of noise, our *Arduino* program used a rolling average of the latest ten samples to determine what we should input into the system. The system relied on the detection of two inputs: load voltage and safety button status. To measure load voltage, we placed a voltage divider in parallel with the load resistor which scaled the voltage down by a factor of five. Reducing the voltage was necessary to stay below the maximum *Arduino Uno* voltage of 5 V. The resistors in the divider were at least 100 kΩ as to consume negligible power and to leave the 3.98 Ω load resistor unaffected.

For the Safety task, the team mimicked a button press using a piece of wire and a simple crimp housing to create a loop that could be disconnected. This wire connected a digital supply pin on the Arduino directly to an analog input pin. When sampling, the supply pin turns on and the input pin normally reads around 5 V. If the loop is disconnected (representing the button press), then a 2.2 kΩ pull down resistor makes the input pin read close to 0 V. The program kept track of this pin as either High or Low and provided thresholds of 0.8 V and 4.2 V for the variable to change between these states.

The Arduino outputs included digital pins used to control the stepper motors responsible for pitch control and the mechanical brake. A Nema-17 bipolar stepper motor (part **(i)** in **Figure 8**) was connected to a linear actuator to control the blade's pitch angle. The team decided to interface both motors using a TI DRV8834 motor driver configured in STEP/DIR mode. This mode was selected because of its ease to control the motors using just three digital inputs. DIR input pin sets the motor to rotate clockwise or counterclockwise, and STEP pin makes the motor step once when provided a rising edge. Both motor drivers were configured to step the motors one full step (1.8°) per rising edge because neither the pitch nor brake system required accuracy finer than this. The SLEEP pin could be toggled to conserve power when it was known the motor would not need to be stepped for a while, such as during the Cut-In, Power Curve and Durability tasks.

We used four digital output pins to control current through the set and reset coil each for the load relay and generator-connection relay. Signals to the load connected to the gate of a MOSFET to make it behave as a switch, and the other two supplied voltage directly across the relay coils. Hardware Abstraction Layers (HAL) functions were called in the program to allow or block current through each coil as needed.

Finite State Machine for Competition Tasks

Table X, in detail, the states of each task, as well as a description of the finite state machine at each task. Additionally, **Figure 15** shows the organization of the finite state machine which organizes the software around the competition tasks. The arrows describe how the inputs determine which task to change to.

Table X. Finite State Machine Functions and Conditions for State Change for Each Task

State	Description and Functions of State	Conditions to Enter State
Cut-in	● Blades pitched and maintained at cut-in angle (22°)	● Arduino turns on and initializes program. ● After exiting safety task
Power Curve	● Blades pitch to optimal power curve angle (15°)	● During cut in and power > 1.7W ● During control of rated power and power < 10W
Durability	● Considered the same as power curve	● Same as power curve
Control Rated	● Maintain output power as close to 15W as possible. ● Uses feedback controller with proportional gain to control blade stepper motor	● During power curve and power > 15W
Safety Button	● Closes the mechanical brake. ● Switches load the battery and disconnects generator when brake is halfway closed. ● Waits until safety button is unpressed	● During cut in, power curve, or control of rated power. ● Safety button pressed: < 0.8V on safety button Arudino pin
Safety Exit	● Opens the mechanical brake ● Switches load to resistor and reconnects generator when brake is halfway opened	● During safety button and Safety button unpressed: >4.2V on safety button Arduino pin

The system enters the Cut-In task immediately after the *Arduino* turns on and initializes the program. To begin the task, the controller pitches the blade to the desired angle using the stepper motor. It then keeps the blades in this position until moving to the next task.

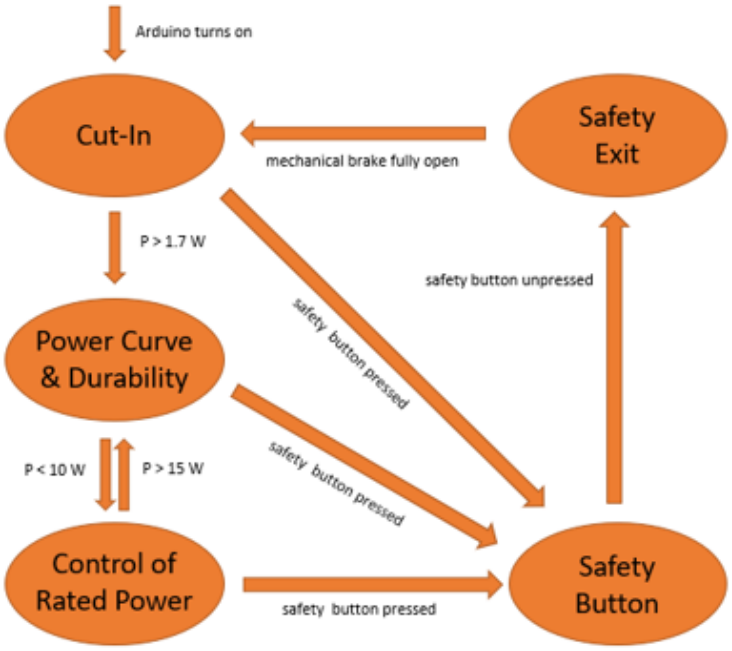

Figure 15. Finite State Machine for Competition Tasks

For the power curve task, the *Arduino* calculates the load power from load voltage using the equation $P = V_{load}^2/R_{load}$. When the load power rises above 1.7 W, the turbine enters the power curve state. When this occurs, the turbine pitches the blades to the power curve angle, the angle determined to be the best angle to produce power at. This year we tested at different pitch angles at all Power Curve wind speeds and chose 15° to be the pitch angle to maximize our points for the Power Curve task by producing the most power at most wind speeds.

The turbine transitions to the Control of Rated Power task state when the load power is above 15 W, the rated power determined from testing. To maintain 15 W above 11 m/s, the turbine uses a digital feedback controller with proportional gain. The *Arduino* calculates the error between the actual load power and reference power (15 W). To increase power, the pitch stepper motor needs to move the aluminum housing (part **(g)** in **Figure 8**) right, and to decrease power it moves the housings left. The larger the error, the more steps the motor is instructed to step in one iteration. Therefore, the sign of the error determines the direction of the stepper motor, and its size determines the number of steps. Additionally, the controller has limitations that ensure that the motor is not stepping past the maximum/minimum limits. Finally, if the power is within ±200

mW, the system decides not to change the pitch angle until the error is outside these bounds. The system will exit this task to the Power Curve task when the load power drops below 10 W.

To complete the Safety task, the system checks for the manual stop “button” being pressed during Cut-In, Power Curve, and Control of Rated Power tasks. If the voltage on the safety button *Arduino* pin drops below 0.8 V, then the system first stops pitching the blades. It then begins to step the brake motor. When the brake is halfway closed, the *Arduino* switches the load relay to battery, and it disconnects the generator from the load, so the battery is not connected to the generator. Once the brake has fully closed and the turbine stops rotating, the system waits in the safety exiting task until the safety button is “unpressed”. When the safety button is unpressed, the *Arduino* begins to open the mechanical brake. When it is halfway opening, it reconnects the generator and switches the load back to the resistor. Finally, when the brake is fully open, the blades pitch back to the cut-in angle and the system enters the Cut-In task. The operation for a load disconnect is very similar. The only difference is that the *Arduino* turns off while the load is disconnected and will return to the Cut-In state when it turns on with a load reconnect.

Durability task did not require its own state in software since the passive mechanical systems would keep the turbine facing into the wind and the turbine would produce positive power between 6 and 13 m/s if it faces into the wind.

Final Testing Results

Prior to the final testing period some additional changes to the controls were made due to certain restrictions on the system and in design time that were discovered in interim testing periods. The results of the final testing period are described in this section.

Cut-In

When testing our turbine, we observed that the chosen cut-in angle of 22° produced very little power and so the pitch control system didn't have enough power to pitch the blades until about 9 m/s. This resulted in near-zero points during the Power Curve task; therefore, we opted to change the cut-in angle to be the same as the power angle (15°). In testing, the turbine’s cut-in wind speed suffered about a 0.5 m/s increase from this change.

Power Curve

Figure 16 shows the power produced during the Power Curve task at the final testing period. The final blade design was chosen because it performed better at all wind speeds than the blade with the shorter chord length. The blades with the longer chord length cut-in before 5m/s and produced higher power than the short-chord blade. The ideal load of 3.98 Ω and performance pitch angle of 15° were chosen to maximize power production at lower wind speeds to obtain the most points during the power curve task.

With these results, we generated another estimate for Annual Energy Production (AEP). Using the same approach described in

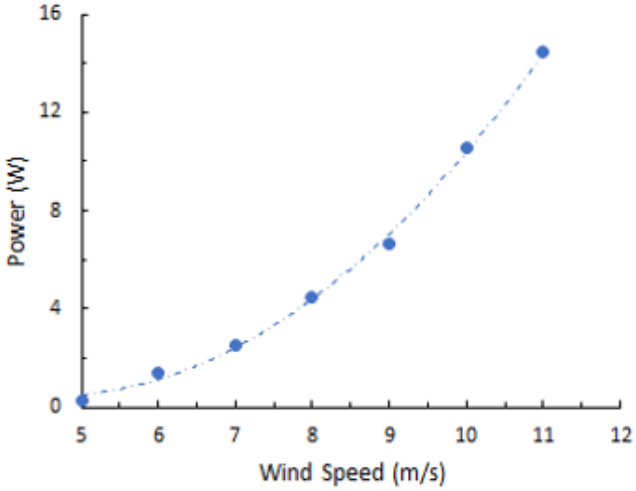

Figure 16. Power curve from final testing period data

the Blades section, we calculated an AEP of 30.013 kWh/year, a significantly smaller amount of energy production.

As indicated by **Figure 16** and our updated AEP, our turbine produced less power in the wind tunnel than we predicted via MATLAB and Qblade analyses. Though the specific reason for this discrepancy is not certain, we believe the reduced power output is due to friction in the mechanical system, wire resistance connecting the load, and inefficiencies caused by vibrations. Small imperfections in the blade's surfaces, due to the hand layup manufacturing process, could have also reduced the turbine's efficiency. Though each blade was made precisely, according to detailed procedures, and weighed throughout production to ensure uniformity, small imperfections are possible.

Control of Rated Power

As the turbine was subjected to wind speeds in the range of 12 m/s and 13 m/s a proportional controller was able to make changes to the pitch angle of the turbine to maintain rated speed and power. During the final testing, the controller was able to pitch the blades to change the angle of attack; however, during the 12 m/s bin the output power would oscillate between 7.78 W and 19.0 W without the ability to converge. The proportional controller was more successful at maintaining a constant, lower power output in the 13 m/s wind speed bin. At this value, wind speed the output values converged on 16.4 W at an RPM of 1100. Success in this portion of the task gives the team confidence that in the future, by using a PID controller in place of a proportional controller the team can accomplish the control of rated power successfully by reducing inherent error associated with P-control.

Safety

While operating at 10m/s, we simulated the button press which activated the movement of the turbine's mechanical brake. The mechanical brake pad was able to move towards the brake disc. However, the brake was unable to stop the turbine in under 10 seconds. The turbine has the capability to complete this task if the braking mechanism moves quicker. To fix this issue, we will need to change the lead screw threading to allow the brake to actuate faster.

The load disconnect was not attempted in the final test because in past tunnel testing the team experienced problems with storing in memory the step position of the two stepper motors. Additionally, it was difficult to predict when the Arduino would turn off once the mechanical brake began to close, so there were concerns the Arduino would lose power before the turbine completely stopped rotating.

Durability

The turbine was able to undergo 5 minutes of testing at various wind speeds ranging from 6 m/s to 13 m/s while being turned out of the wind. This task was mainly completed by the passive yaw system which kept the turbine always facing into the wind, allowing the turbine to continuously produce positive power.

Appendix A - Blade Spar Loading Calculations

Table A1. Axial Loading Constants

r_h , $hub\ radius$	ω	A_{hole}	ρ_l	l_{blade}
$0.0125\ m$	$345.6\frac{rad}{s}$	$9.56 * 10^{-5}\ m^2$	$0.3302\ \frac{kg}{m}$	$0.17\ m$

$$\frac{dF_x}{dx} = (r_h + x)(\rho_l)(\omega^2)$$

$$F_x = \int_0^{l_{blade}} (r_h + x)(\rho_l)(\omega^2)dx \ = \ 653.3148\ N$$

$$\sigma_x \ = \frac{F_x}{A_{hole}} = 6.8338 * 10^6\ Pa$$

Table A2. Aerodynamic Loading Constants

$U_{\infty,wind\ speed}$	ω	$a_{axial\ induction}$	$a'_{tan\ induction}$	$c_{chord\ length}$	C_{lift}	C_{drag}
$25\ \frac{m}{s}$	$345.6\ \frac{rad}{s}$	$-0.3227\ m^2$	$-0.1098\ \frac{kg}{m}$	$0.2148\ m$	0.688	0.00708

$\alpha_{angle\ of\ attack}$	β_{twist}	θ_{pitch}	r_h , $hub\ radius$	ρ_{air}
3.5°	28.85°	15°	$0.0125\ m$	$1.225\ \frac{kg}{m^3}$

$$V_{rel} \ = \int_0^{l_{blade}} \sqrt{{U_\infty}^2(1-a)^2 + \omega^2 r^2(1+a')^2}\ dx, where\ r \ = x \ + r_h$$

$$L' \ = C_l(\frac{1}{2}\rho_{air}{V_{rel}}^2)c$$

$$D' \ = C_d(\frac{1}{2}\rho_{air}{V_{rel}}^2)c$$

$$F_y \ = L'sin(\alpha+\beta+\theta) - D'cos(\alpha+\beta+\theta) = 4.0531\ N$$

$$F_z \ = L'cos(\alpha+\beta+\theta) + D'sin(\alpha+\beta+\theta) = 3.8114\ N$$

$$\sigma_y \ = \frac{F_y}{A_{hole}} = 4.2397 * 10^4\ Pa$$

$$\sigma_z \ = \frac{F_z}{A_{hole}} = 3.9868 * 10^4\ Pa$$

$$\sigma_{resultant} = 6.8341\ MPa$$

$$\boldsymbol{n} \ = \frac{\boldsymbol{\sigma_{yield,Al}}}{\boldsymbol{\sigma_{resultant}}} = \frac{\mathbf{241}}{\mathbf{1.413}} = \mathbf{35.2644}$$

Appendix B -

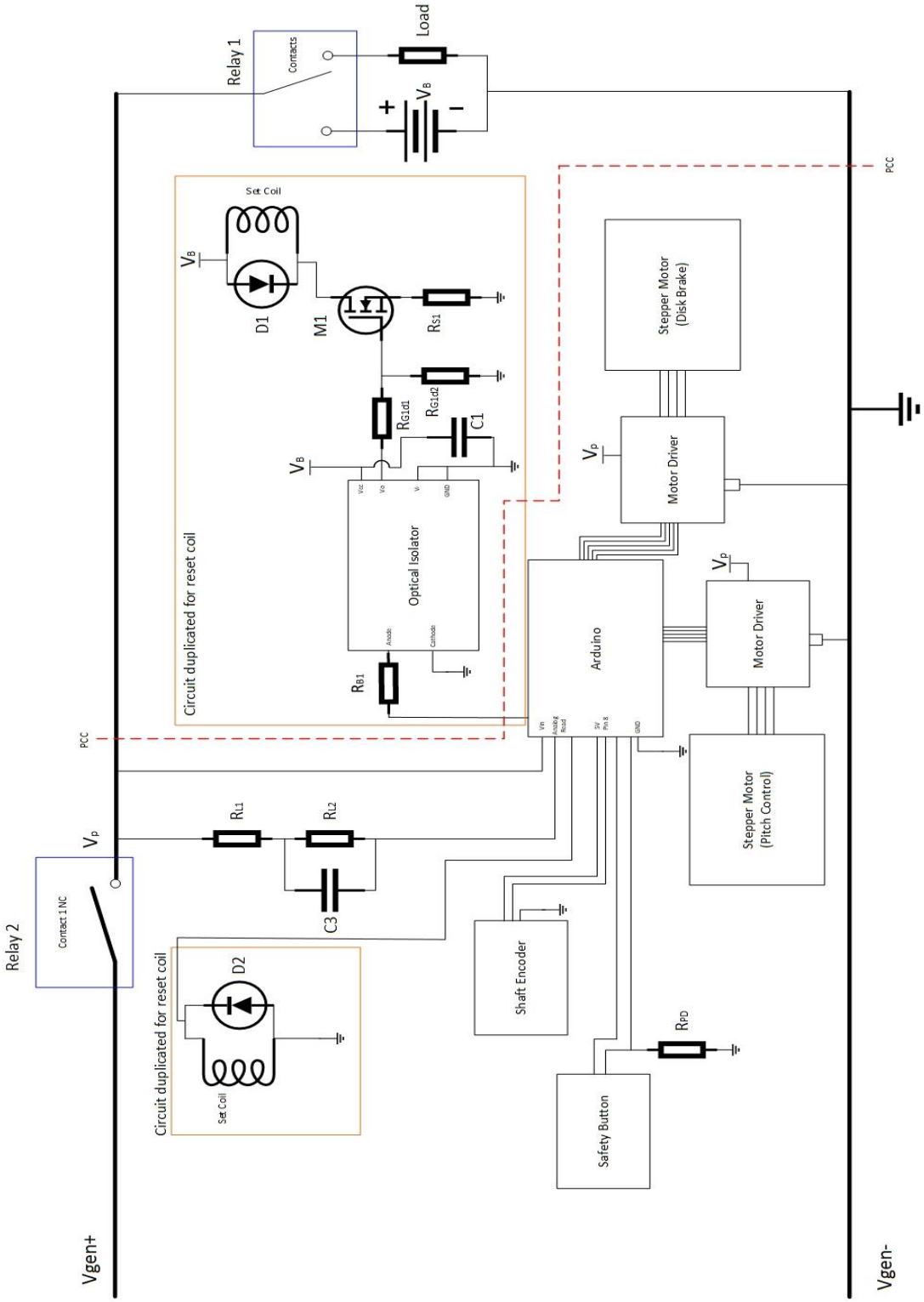

Figure B1. Full system schematic. Voltage across load was about 7.5 V at 11m/s.

References

[1] E. Kulunk, “Aerodynamics of Wind Turbines,” in *Fundamental and Advanced Topics in Wind Power*. New Mexico Institute of Mining and Technology, 2011.

[2] A. Maheri, S. Noroozi, C. Toomer, J. Vibbey, “Damping the fluctuating behaviour and improving the convergence rate of the axial induction factor in the BEMT- based rotor aerodynamic codes,” University of the West of England, 2006.

[3] S. A. Ning, “A simple solution method for the blade element momentum equations with guaranteed convergence,” National Renewable Energy Laboratory.

[4] W. Z. Shen, R. Mikkelsen, J. N. Sorensen, “Tip Loss Corrections for Wind Turbine Computations,” Department of Mechanical Engineering, Technical University of Denmark, 2005.

[5] J. S. Arora, *Introduction to Optimum Design*. 2017.

[6] M. O. L. Hansen, *Aerodynamics of Wind Turbines*. Routledge, 2015.

[7] *The Wind Prospector*, NREL. [Online]. Available: https://maps.nrel.gov/wind-prospector/ (accessed Apr. 23, 2021).

[8] D. J. Inman, in *Engineering Vibration*, Pearson, 2014, pp. 117–142.